An Online ACB-index: Quantifying Intraseasonal and Interannual Variability in Mars' Aphelion Cloud Belt

M. Mester[1], J. M. Battalio [2], R. J. Wilson [3], M. A. Kahre [3]

[1]HUN-REN ELTE Theoretical Physics Research Group, Budapest, Hungary
[2]Department of Earth and Planetary Sciences, Yale University, New Haven, CT, USA
[3]NASA Ames Research Center, Mountain View, CA, USA

Key Points:

- An online Aphelion Cloud Belt index is introduced to quantify and track intraseasonal variability in Mars' tropical water-ice clouds.
- The ACB-index provides a compact descriptor of episodic west-east shifts in cloud abundance between Tharsis and Syrtis Major.
- The first shift of each Mars Year is locked to the seasonal cycle, whereas subsequent shifts are more irregular and transient.

Corresponding author: Marton Mester, `mester.marton@ttk.elte.hu`

Abstract

Mars' Aphelion Cloud Belt (ACB) is a recurrent tropical water-ice cloud system central to the seasonal water cycle, but its intraseasonal variability remains poorly quantified. Recent work identified large-scale oscillations involving episodic shifts in cloud abundance from Tharsis toward Acidalia and then Syrtis Major, sometimes termed the Tropical Cloud Oscillation, but these events remain difficult to define objectively. We use blue-filtered Mars Daily Global Maps (MDGMs) from MRO/MARCI during $L_s = 0-180^\circ$ in MY 28-35 to construct an empirical, low-dimensional description of ACB variability at approximately 3 pm local time. After spatial binning, we apply empirical orthogonal function (EOF) analysis of the tropical blue-channel field. Before constructing the EOF basis, we remove two localized eastward-propagating spectral artifacts associated with MRO's twice-daily observation pattern. The leading EOFs capture the dominant Tharsis-centered cloud maximum and episodic reorganization toward Acidalia and Syrtis Major. We define an online ACB-index from normalized principal component anomalies in phase-amplitude form, providing a quantitative measure of the timing, amplitude, and life cycle of west-east cloud shifts across Mars Years. The first major transition in each year occurs within a narrow L_s window and is therefore consistent with a seasonally controlled adjustment of the quasi-stationary tropical circulation. Later transitions are less repeatable, vary strongly in amplitude and duration, and are better described as transient intraseasonal events. The proposed ACB-index therefore separates the repeatable seasonal component of the ACB evolution from year-specific episodic variability, providing a practical framework for comparing observations, reanalyses, and Mars global climate model simulations.

Plain Language Summary

Every northern spring and summer on Mars, a band of water-ice clouds forms near the equator. This is called the Aphelion Cloud Belt. Although the cloud belt appears every year, its detailed structure changes from day to day and from year to year. Sometimes the cloudiest region lies near the large volcanic province of Tharsis, while other times clouds weaken there and strengthen farther east, near the shield volcano Syrtis Major. In this study, we develop a quantitative way to track these cloud shifts using daily global images of Mars. We reduce the complicated cloud maps to a small number of dominant spatial patterns and then use their time evolution to define an Aphelion Cloud Belt index. This index shows when the cloud belt shifts, how strong the shift is, and whether

the event resembles shifts in other Mars Years. We find that the first major shift each year starts within the same 5-10 days, suggesting that it is controlled by the regular seasonal evolution of Mars' climate. Later shifts are less predictable and appear to behave more like transient weather-like events.

1 Introduction

The Aphelion Cloud Belt (ACB) is a tropical water-ice cloud system on Mars that is present between the northern vernal and autumnal equinoxes (at $L_s = 0°$ and 180°, respectively; L_s denotes solar longitude), and attains its maximum in cloud abundance in the season after aphelion (occurring at $L_s = 71°$). The ACB plays an important role in the present-day water cycle by modulating vertical and meridional water-vapor transport (Clancy et al., 1996; Montmessin et al., 2004; Madeleine et al., 2012; Smith, 2019; Guha et al., 2021). Through radiative feedbacks it influences tides (Hinson & Wilson, 2004; Wilson et al., 2008; Wilson & Guzewich, 2014; Wilson et al., 2014), and the Hadley-cell (Richardson et al., 2002; Kahre et al., 2015). Although often described through its zonal mean seasonal evolution (Clancy et al., 1996; Smith, 2004; Montmessin et al., 2004; Wolff et al., 2019; Guha et al., 2021), the ACB exhibits substantial intraseasonal and longitudinal variability (Khayat et al., 2023; Willame et al., 2026). A dominant component of the intraseasonal variability is the episodic shift of tropical cloud abundance between Tharsis and Syrtis Major provinces (Wang & González Abad, 2021; Wang et al., 2024; Lemmon et al., 2025; Mester, Wilson, & Kahre, 2026).

Recent work has referred to this cloud shift as the Tropical Cloud Oscillation (TCO) (Wang & González Abad, 2021), emphasizing the apparent large-scale, recurrent displacement of tropical cloud abundance between preferred longitudinal sectors. Although planetary-scale water-ice cloud systems are well understood to influence atmospheric circulation (see above and corresponding references), the extent to which different TCO phases alter climate remains unclear and undetermined. This shortfall stems from several factors, including the recency of TCO pattern identification by Wang and González Abad (2021) and the lack of clear definitions for the TCO's spatial structure, phase, timescale, amplitude, and variability.

In particular, despite its visual prominence, the TCO has not yet been defined in a fully objective or quantitative manner from observations. Its period is described broadly

(10-40 sols by Wang and González Abad (2021); Wang et al. (2024), where sol = 1 Martian day), the distinction between a single prolonged event and multiple recurrent events within the same Mars Year is not always clear (Wang et al., 2024), and the degree to which the phenomenon repeats from year to year remains incompletely characterized. As a result, it is difficult to compare TCO events across Mars Years, to determine whether a given year contains one or several shifts, or to evaluate the extent to which a model simulation reproduces the observed behavior (Mester, Wilson, & Kahre, 2026).

The observation-based characterization of the TCO has been exclusively treated as a combination of modes with constant wavenumber and frequency (Wang et al., 2024); however, global climate modeling suggests that slow variability (i.e., period $>$ 20 sol on the wavenumber-frequency spectrum) may be better captured by empirical orthogonal function (EOF) diagnostics (Mester, Wilson, & Kahre, 2026). Here we further analyze ACB interannual variability by determining the leading modes of variability (i.e., EOFs) from once-daily spacecraft observations and associate the TCO with a selection of EOFs. Furthermore, we design and propose an online ACB-index that aims to define a phase-amplitude metric for intraseasonal and longitudinal variability of the Aphelion Cloud Belt. We show that the ACB-index is a good quantitative descriptor of the Tharsis-Syrtis Major cloud shift that can be used to consistently evaluate the timing, periodicity, and amplitude of each shift. Furthermore, the index can be used to compare and contrast the interannual variability in the Tharsis-Syrtis Major cloud shift.

We distinguish between offline and online formulations of the ACB-index, following the terminology used for real-time atmospheric indices (e.g., Wheeler & Hendon, 2004). The offline formulation is calculated retrospectively using the complete observational record, including year-specific seasonal means, and is therefore most suitable for studying past ACB variability. The online formulation instead uses previously determined EOFs and climatological statistics to calculate the ACB-index from daily information, without requiring future observations or recalculating the EOFs. Although the online formulation approximates the offline results, it allows the index to be calculated as new observations become available, making it more suitable for routine monitoring and potential forecasting applications. Hence, online and offline refer to the calculation methods rather than the availability of the resulting data products.

The paper is organized as follows. Section 2 describes the dataset used, and the construction of the ACB-index. Section 3 presents the evolution of the ACB-index for Mars Years 28-35 during $L_s = 0{-}180°$, and the spatio-temporal evolution of the TCO is discussed, including timescales, phase-amplitude evolution, number of shifts, and interannual variability. Section 4 discusses the physical interpretation of the results, including the distinction between seasonally locked and transient TCO components. Section 5 summarizes the conclusions.

2 Data and Methods

2.1 Mars Daily Global Maps

We analyze Mars Daily Global Maps (MDGMs, Wang et al. (2020)) constructed from Mars Reconnaissance Orbiter (MRO) Mars Color Imager (MARCI) observations. Each sol, apart from periods of missing data, the MDGMs provide near-global daily coverage at approximately 3 pm local time. This fixed local time is advantageous for constructing a consistent daily record, but it also means that the analysis samples one phase of the diurnal cycle rather than the full diurnal evolution of the cloud field (Giuranna et al., 2021).

The pre-scaled, photometrically corrected blue-filter component of the MDGMs (expressed as unitless pixel values) has been used to analyze water-ice clouds and the TCO by Wang et al. (2024, W24 hereafter) after they demonstrated that blue-channel brightness strongly correlated with UV water-ice cloud opacity. Since the pre-scaled images used by W24 are not publicly available, here we obtain blue-filter fields from the RGB MDGMs instead (available at Wang et al. (2020)). The resulting blue-channel brightness in our analysis is simply a constant multiple of W24's, and this arbitrary scaling does not affect correlation with UV water-ice cloud opacity, the TCO phase structure or timing of the cloud variations.

We bin the blue-filter MDGMs to a $2.5° \times 0.5°$ longitude-latitude grid, and restrict the analysis to the tropical band from 30°S to 30°N, which contains the dominant ACB signal and reduces contamination from higher-latitude seasonal cloud systems. The spatial binning to a more crude resolution is done to reduce computational burden in the subsequent empirical orthogonal function analysis, see below, from a requirement of more than 100 GB to a few hundred MBs of RAM. Additionally, the exact binning resolution

we use matches the longitude-latitude resolution used by W24 who argued that this resolution sufficiently mitigates the influence of residual image processing artifacts. Spatial linear interpolation on a Delaunay triangulation is used to fill limited missing regions in individual maps when necessary. This gap filling method is different from W24's; however, they suggested that their results are insensitive to the gap filling method. In addition, we validated linear interpolation by artificially masking observed regions of three sizes (5×5, 11×11, and 21×21 grid cells), finding 27–53% lower reconstruction errors than with OpenCV image inpainting.

2.2 Empirical orthogonal function construction

We determine the leading modes of ACB intraseasonal variability by performing an empirical orthogonal function (EOF) analysis (for a detailed description of the method see e.g., Hannachi et al., 2007) that has been used extensively in terrestrial tropical atmospheric dynamics (Matthews, 2000; Wheeler & Hendon, 2004) and has established presence in Mars atmospheric literature (see e.g., Leroy et al., 2003; Yamashita et al., 2007; M. J. Battalio & Lora, 2021; J. M. Battalio et al., 2025; Mester, Wilson, & Kahre, 2026). The EOFs are calculated from blue-channel brightness anomalies (with respect to the seasonal mean at each year), constrained to the tropics between 30°S and 30°N. We calculate the covariance matrix of blue-channel brightness over time from a spatial vector obtained by vectorizing each longitude-latitude map. This is done by taking each column of the image one by one and concatenating them into a single column before stitching them into a location-by-time array. The eigenvectors of the covariance matrix of the location-time array are then unwrapped back into longitude-latitude images.

These unwrapped images correspond to the spatial patterns (EOFs) and the projection of an MDGM at any time to an EOF results in its respective principal component (PC). We normalize the EOFs so that the summed point-wise amplitude squared equals 1.

In our analysis, we calculate the EOFs and PCs from blue-filter MDGMs for latitudes between 30°S and 30°N during MY 28-35, $L_s = 0 - 180°$. The MDGM record starts at $L_s = 132°$ in MY 28, so the first analyzed year is incomplete.

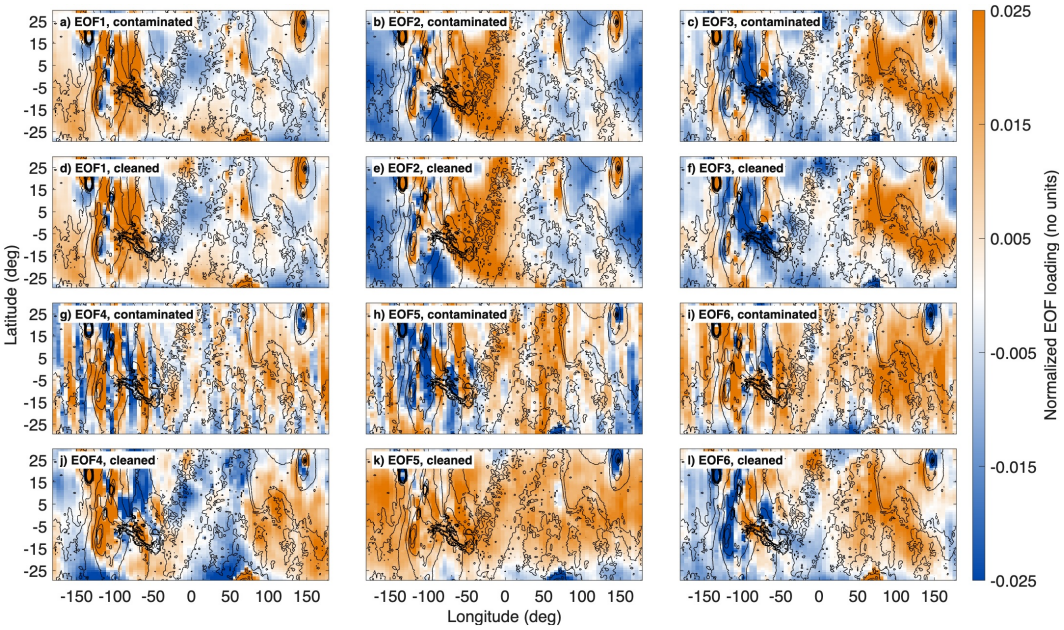


Figure 1: EOF patterns before (a-c, g-i) and after (d-f, j-l) ghost signal removal. The normalized EOF patterns are displayed in color, with topography overlaid in black.

3 Results

3.1 Spatial pattern and seasonal evolution of the leading modes of variability

For geographical reference, the main regions discussed below are Tharsis (approximately 140-60°W), Acidalia (around 20°W), and Syrtis Major (around 70-100°E), with these longitudes denoting broad geographical sectors rather than sharply defined boundaries.

The EOF analysis reveals that the leading modes (see Fig. 1) of 3 pm tropical cloud variability include a dominant pattern that describes high cloud cover over Tharsis (EOF1, 26.6% explained variance, Fig. 1a), a pattern that corresponds to cloud amplification over Acidalia (EOF2, 7.2% explained variance, Fig. 1b), and a Syrtis Major - Tharsis asymmetry (EOF3, 4.6% explained variance, Fig. 1c)).

Interpreting higher EOFs is less straightforward, as a consistent wavenumber 11-13 pattern contaminates the EOF structure (EOFs 4-6 shown in Fig. 1g-i). This ghost signal arises from how MDGMs are constructed: they are stitched together from mul-

tiple image swabs taken approximately 2 hours apart from successive MRO orbits. W24 also reported this ghost signal, showing that the wavenumber-frequency spectrum is strongly contaminated by it. This contamination prevented them from performing the method of background spectrum removal in their search for Kelvin or Rossby wave-associated spectral bands. Therefore, removing this ghost peak is imperative if one aims to analyze ACB variability, irrespective of whether the analysis builds on EOF construction or on wavenumber-frequency analysis. In what follows, we describe a method for removing this ghost signal. Upon the removal of the ghost signal, we will illustrate that EOFs 4-6 become 'cleaned up' with no strong wavenumber 11-13 contaminating the patterns any longer.

3.1.1 Ghost signal removal

In order to remove the contaminating structure from the blue-channel brightness $B(\lambda, \theta, t)$ record (λ is longitude, θ is latitude, t denotes time), first we must identify the most prominent peaks of the ghost signal in the wavenumber-frequency spectrum. We determine the mean spectrum of B by latitudinally averaging the multi-year-averaged wavenumber-frequency spectrum obtained from MY 28-35 (Fig. 2a). We find that the two strongest ghost peaks are at wavenumbers 11 and 13, with a frequency of approximately 0.185 cycles per sol (cps), consistent with the spectrum determined by W24, and a more specific 3/16 (= 0.1875) cps frequency pointed out in Hinson and Wilson (2021) as a harmonic of the repeat cycle of MRO's orbit.

For each Mars Year and latitude θ, the longitude-time anomaly in blue-channel brightness $B_\theta(\lambda, t) = B(\lambda, \theta, t)$ is Fourier-transformed, formally written as

$$\widehat{B}_\theta(k, f) = \mathcal{F}_{\lambda,t}\left\{B_\theta(\lambda, t)\right\}. \tag{1}$$

In Fourier space, we aim to remove the two identified ghost peaks and their complex-conjugate counterparts to preserve a real-valued inverse transform. Therefore, we consider the target peaks centered at $(k_0, f_0) = (13, 0.185)$ and $(k_0, f_0) = (11, 0.185)$, with their complex counterparts at $(k_0, f_0) = (-13, -0.185)$ and $(k_0, f_0) = (-11, -0.185)$, where k is zonal wavenumber and f is frequency in cps. For each target peak, a broad center-weighted spectral mask is defined over $k \in \pm[3, 23]$, $f \in \pm[0.06, 0.26]$ cps. Within these rectangular neighborhoods, the mask is weighted by a Gaussian centered on the

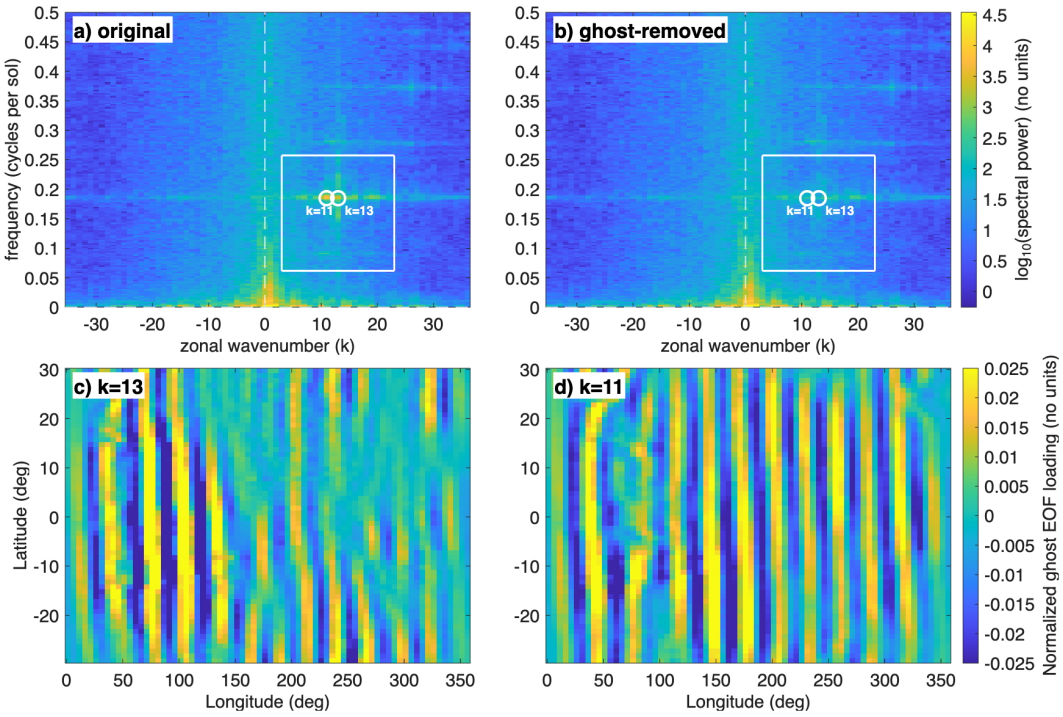


Figure 2: Details of ghost signal identification. *Top*: Wavenumber-frequency spectrum before (a) and after (b) ghost signal removal. White circles denote the locations of dominant ghost peaks in the original spectrum. The white rectangle shows the neighborhood in which an exponential weight is applied and ghost EOFs are calculated. *Bottom*: Ghost EOF1s calculated from masks with exponential weight centered at $k = 13$ (c) and $k = 11$ (d).

target ghost peak:

$$M(k,f) = \exp\left[-\frac{1}{2}\left(\frac{k-k_0}{\sigma_k}\right)^2 - \frac{1}{2}\left(\frac{f-f_0}{\sigma_f}\right)^2\right]. \tag{2}$$

The mask is set to zero outside these neighborhoods. The Gaussian parameters are chosen empirically as $\sigma_k = 4$ and $\sigma_f = 0.08$ cps.

The ghost-band component (indicated by left-superscript g) was reconstructed by multiplying the shifted Fourier coefficients by the ghost mask and transforming back to physical space:

$${}^{g}B_{\theta}^{\boldsymbol{k_0}}(\lambda,t) = \mathcal{F}^{-1}_{\lambda,t}\left\{M(k,f)\widehat{B}_{\theta}(k,f)\right\}, \tag{3}$$

where $\boldsymbol{k_0} = (k_0, f_0)$. This operation is repeated independently for all (tropical) latitudes and Mars Years, producing a three-dimensional ghost-band reconstruction $G_{\boldsymbol{k_0}}(\lambda,\theta,t)\{B\} = {}^{g}B_{\theta}^{\boldsymbol{k_0}}(\lambda,t)$ from B for each target ghost centred at $\boldsymbol{k_0} = (13, 0.185), (11, 0.185)$. For simplicity, we will use the shorthand $G_k = G_{(k,0.185)}$.

Next, we identify and remove dominant ghost-peak signals within the ghost bands sequentially. First, the $(k,f) = (13, 0.185)$ ghost-band field $G_{13}\{B\}$ is reconstructed from the original anomaly field B. The first two EOFs in $G_{13}\{B\}$ and their principal components are calculated and used to reconstruct the dominant ghost contribution,

$$G_{13}^{(1,2)}(\lambda,\theta,t)\{B\} = \sum_{m=1}^{2} \mathrm{PC}m_{G_{13}\{B\}}(t)\,\mathrm{EOF}m_{G_{13}\{B\}}(\lambda,\theta). \tag{4}$$

The one-ghost-removed signal is then calculated as

$$B^1(\lambda,\theta,t) = B(\lambda,\theta,t) - G_{13}^{(1,2)}(\lambda,\theta,t)\{B\}. \tag{5}$$

The same procedure is then repeated for the $(k,f) = (11, 0.185)$ ghost peak (and its complex conjugate), with the ghost contribution $G_{11}^{(1,2)}\{B^1\}$ calculated from the residual B^1 instead of B. The resulting two-ghost-removed signal is given by

$$B_{\mathrm{clean}}(\lambda,\theta,t) = B(\lambda,\theta,t) - G_{13}^{(1,2)}(\lambda,\theta,t)\{B\} - G_{11}^{(1,2)}(\lambda,\theta,t)\{B^1\}. \tag{6}$$

Upon removal of the two ghosts, the new wavenumber-frequency spectrum no longer contains strong peaks at $k = 11, 13$ (Fig. 2b). The removal mostly weakens the spectrum in the wavenumber range $k = 11-13$ across a broader frequency range, and the 0.185 cps frequency still shows relatively high power at all wavenumbers. Since the removed EOF is constrained to within a fixed neighborhood (white rectangles on Fig. 2a,b), the spectrum is not modified outside the region. Fig. 2c,d shows the two ghost EOF1s, which

are mostly composed of wavenumber 11, 12, and 13 components, with some zonal amplitude asymmetries. We note that the corresponding EOF2s are quadrature pairs of EOF1s, therefore not shown.

3.1.2 Intraseasonal and interannual variability of the ACB after ghost signal removal

We follow our analysis by recalculating the EOFs from the cleaned blue-channel brightness record B_{clean} for MY 28-35 over $L_s = 0{-}180°$. The resulting ghost-free spatial patterns of EOFs 1-6 are shown in Fig. 1d-f, j-l. The reader should note that the EOFs are organized by explained variance, and the ghost signal may have explained a different variance in each EOF. Therefore, EOFk before ghost removal and after may not correspond to the same physical pattern for each k. In particular, the results suggest that while EOFs 1-4 correspond to the same structure before than after the ghost removal, EOFs 5 and 6 are exchanged by the ghost removal. We can now interpret the spatial structure of the EOFs obtained from the cleaned blue-channel brightness record.

The results reconfirm that the first 3 EOFs from the uncleaned data (Fig. 1a-c) were not notably contaminated by the ghost signal; now, EOFs 1-3 explain 27.9%, 7.7%, and 4.7% variance, respectively. However, the originally heavily wavenumber 11-13-influenced EOFs 4-6 are successfully cleaned of ghost-signal contamination, providing evidence for the effectiveness of our method. EOFs 4-6 explain 2.9%, 2.5% and 2.2% variance. The analysis shows that EOF4 corresponds to a highland-lowland asymmetry, i.e., amplification over Tharsis and Syrtis and weakening over Acidalia and Arcadia, or vice versa. EOF5 corresponds to a universal strengthening of cloud abundance over the tropics, and EOF6 can be interpreted as a Syrtis amplification accompanied by a western Tharsis weakening and eastern Tharsis strengthening.

We restrict our analysis to the first six EOFs to capture both the dominant and secondary spatial patterns of ACB variability. While EOFs 1-3 describe the principal cloud abundance variations over Tharsis, Acidalia, and Syrtis Major, EOFs 4-6 reveal additional structures associated with regional asymmetries and changes in tropical cloud abundance. The first six EOFs are therefore examined to characterize these secondary patterns and illustrate the influence of the ghost signal on higher-order EOFs. This choice

does not represent a statistical significance threshold, and higher-order modes are not considered further as they are beyond the scope of the present analysis.

We test the stability of the EOF patterns by recalculating the EOFs after leaving out a Mars Year (for each of MYs 28-35). Among the first 12 EOFs, we find that only EOF8 and EOF9 switch order (i.e., EOF9 attains higher explained variance than EOF8), and they do so when either MY 30 or MY 35 is left out. Furthermore, we find that the spatial correlation of EOFa under various MY removals exceeds 0.98 for $a = 1{-}4$. These results suggest that EOFs 1-7 are well separated by the full, 8-year record, and the order of these EOFs is not likely to change when the EOFs are recalculated from a longer MDGM record. Furthermore, EOFs 1-4 are consistent across years with no transient year dominating their pattern.

Having clarified the spatial patterns of the 6 most dominant modes of variability, we now address their evolution over time, across various Mars Years. For each B_{clean}-based EOFk, we consider the associated principal component (or amplitude) PCk. For each PCk, we first calculate the 5-sol causal mean to suppress noise and measurement inaccuracies, and then normalize by the mean and standard deviation across all years and sols in the $L_s = 0 - 180^\circ$ period; the resulting normalized PC evolutions, which we specify as 'offline' PCs, are exhibited in Fig. 3. We refer to the obtained PCs as 'offline', since the construction of them at any time requires information about future cloud cover statistics. Such construction requires knowledge of the multi-year mean and standard deviation, and requires knowledge of the entire seasonal evolution itself so that seasonal anomalies, and subsequently EOFs and PCs, can be calculated.

To facilitate interpretation, the EOFs represent spatial patterns of cloud-brightness variability (Fig. 1), while their corresponding PCs describe how strongly these patterns are expressed over time (Fig. 3). Since the PCs are normalized by their mean and standard deviation, values of +1, 0, and -1 correspond to one standard deviation above the mean, the mean itself, and one standard deviation below the mean, respectively. For example, EOF1 (Fig. 1d) represents enhanced cloud abundance over Tharsis, so decreasing PC1 values indicate a weakening of this cloud pattern relative to its mean expression. Negative PC values therefore do not imply negative cloud abundance, but rather a weaker expression of the corresponding EOF pattern relative to its mean.

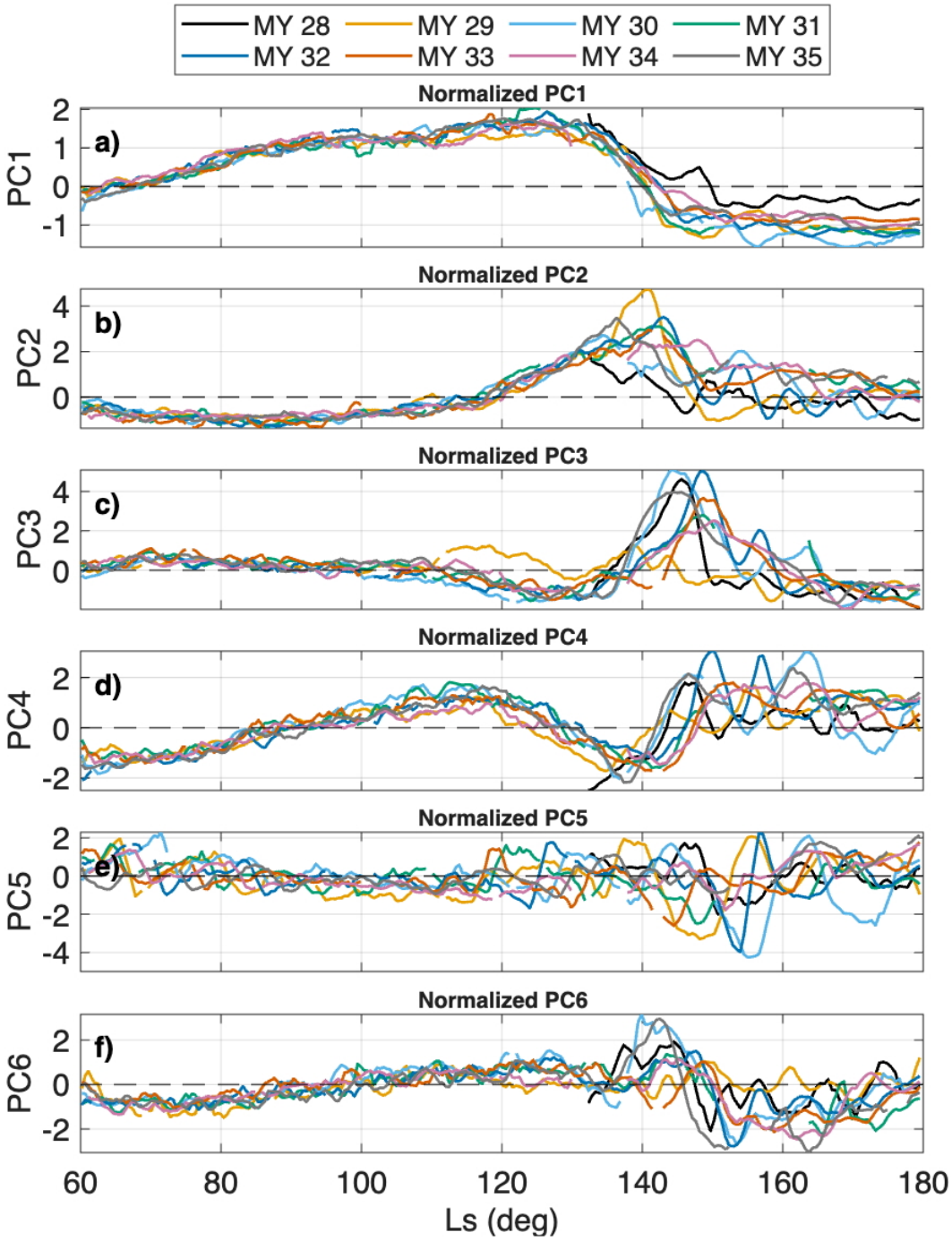


Figure 3: Normalized principal components PC1-6 (a-f) determined from ghost-signal-removed blue-channel brightness for MY 28-35 during $L_s = 60 - 180°$.

We find that PC1, corresponding to cloud abundance over Tharsis, shows very robust interannual behavior; apart from MY 28, the amplitude follows a clear trend with little variability. PC1 amplifies gradually, at a steady rate until $L_s \sim 126°$, followed by a sharper, albeit not too abrupt, weakening. The amplitude consistently hits the 1 std mark between $L_s = 133 - 137°$, and crosses 0 during the period $L_s = 138 - 142°$ (apart from MY 28), showcasing that the temporal room for variations in PC1 is capped around 4 L_s, about 8 sols. After the 0 crossing, PC1 continues to weaken, eventually reaching -1 std by $L_s = 152°$ at the latest, although the rate of weakening shows some interannual variability in this phase. The overall evolution of PC1 suggests that its gradual increase and subsequent weakening are deterministic and are controlled by the seasonal cycle until around $L_s = 142°$, when some transient behavior may influence PC1, although not significantly. Therefore, the analysis suggests that Tharsis cloud amplification and weakening is a gradual process governed by quasi-stationary circulation, with no clear indication of wave influence or transient behavior.

The EOF2 signal, i.e., an Acidalia cloud cover abundance, is weak and negative until around $L_s = 115°$, when PC2 starts a gradual increase that is consistent across the years until 2 std amplitude at $L_s = 131°$. At this time and amplitude, the PC2 signal is already indicating high cloud abundance. During this increase, PC1 remains relatively constant, suggesting that the Acidalia cloud increase may not result from a weakened Tharsis. After $L_s = 131°$, there are significant interannual differences observed in PC2. The amplitude and the timing of the peak vary over MYs. In the most extreme case, PC2 reaches 4 std at $L_s = 140°$ in MY 29; however, in MY 28 and MY 30 the peak occurs even before $L_s = 135°$, and the peak amplitude barely exceeds 2 std. In most years, PC2 has only one peak, although the peak duration may last only a few sols (e.g., MY 35) or several weeks (MY 34). When two peaks are present, the second peak is significantly weaker than the first (MY 30, 32), and in some years we cannot conclude (due to lack of MGDMs) whether a second peak occurred (MY 35), although in MY35 PC2 was increasing before the data gap and decreasing after, suggesting that potentially a second peak was present around $L_s = 155°$. The timing of the second peaks in MY 30, MY32, and potentially MY35 are consistent; however, the sample size is clearly too low to conclude causality. Overall, the results suggest that Acidalia amplification is governed by the quasi-stationary circulations until $L_s = 131°$, when the cloud cover over Acidalia is already significant. The exact duration and amplitude of the amplification is de-

cided by transient processes that take over and result in a less predictable PC2 evolution in the following weeks.

The third most dominant mode of variability, a Tharsis-Syrtis asymmetry, is practically absent, with a near-zero PC3 until $L_s = 110{-}115°$, after which it becomes slightly negative and recovers to zero levels by $L_s = 135 - 138°$. Apart from MY 29, PC3 follows this trend closely every year. Once PC3 turns positive, it amplifies rapidly, manifesting as intensified cloud cover over Syrtis Major, and shows considerable interannual variability in duration, peak time, and peak amplitude. Its peak exceeds 2 std every year except MY 29, with peak times spanning a wider time window $L_s = 143 - 150°$, and peak amplitudes ranging from slightly above 2 std (MY 31, 34) to 5 std (MY 30, 32). The duration of PC3 exceeding 2 std may range from approximately 12 (e.g., MY 32) to 24 sols (e.g., MY 30). Perhaps surprisingly, the weakest year for PC3 (MY 29) coincides with the strongest PC2 peak. The important implication of MY 29 events is that one cannot predict high-amplitude Syrtis Major cloud events based on Acidalia cloud intensification. PC3 evolution also lets us determine whether multiple Syrtis Major cloud amplifications occurred in a year, and lets us compare secondary events with primary ones. We find only two years with a clear second amplification (MY 30, 32) and two further years where further amplifications cannot be determined due to missing MDGMs (MY 31, 35). In the case of MY 30, the two peaks are separated by approximately 40 sols; this separation is only 16 sols in MY 32. In MY 31, the PC3 gradient is negative when MDGMs become available at $L_s = 163°$ after a period of missing data, suggesting a second peak may have occurred shortly before. In MY 35, a second peak is possible, although we do not detect any such signals as for MY 31.

The highland-lowland asymmetry, captured by EOF4 and its amplitude PC4, starts negative at $L_s = 60°$, becomes gradually positive, peaks around $L_s = 115°$ at 1 std, then gradually weakens until $L_s = 137 - 142°$. Until this point, PC4 follows a clear trend with some interannual variability in amplitude; however no anomalous peaks are apparent in any year. After this trough, PC4 becomes positive and amplifies, with peak times matching peak times of PC3. This suggests that Syrtis Major cloud intensifications project onto two modes: one corresponding to opposite Syrtis-Tharsis cloudiness (EOF2) and one to same-signed anomaly (EOF4). Unlike PC3, the secondary peaks in PC4 are of similar magnitude to the first peaks. Therefore, while the first Syrtis Major cloud events occur when Tharsis clouds weaken, the second Syrtis cloud amplification

is accompanied by a secondary recovery at Tharsis. The amplified PC4 after $L_s = 160°$ suggests a second Syrtis event in MY 35; however, we can deduce no new information regarding MY 31.

Unlike PC1-4, which all lack interannual variability until about $L_s = 135{-}140°$, PC5 (an overall tropical cloud intensification) oscillates around 0 std during the entire $L_s = 60 - 180°$ time period. The deviations are mostly negligible until $L_s = 120°$, when the cycles amplify, and PC5 starts to oscillate between $\pm$ 2 std. This nature of oscillations lasts until $L_s = 160°$, with occasional extra amplifications in some years, and after $L_s = 160°$ PC5 continues to oscillate between 0 and 2 std.

Finally, the 6th mode of variability follows a fixed evolution until $L_s = 120°$, with weak variability until $L_s = 137°$. Then, a period of positive peaks, corresponding to Syrtis clouds, (except from MY 33) is followed by a negative period with comparable peaks.

Overall, the structure of each of the first 6 modes of variability in the ACB is robust with little-to-no interannual variability until approximately $L_s = 131°$. Up to that date, ACB evolution is dominated by Tharsis cloud amplification until $L_s = 100°$, followed by plateauing accompanied by Acidalia cloud intensification starting at $L_s = 120°$.

After $L_s = 131°$, the Tharsis clouds weaken gradually with no interannual variability. Acidalia clouds typically strengthen further after this date; however, peak amplitude and timing are inconsistent across years. Acidalia cloud abundance peaks are typically, but not always, followed by strong Syrtis Major cloud intensification, which shows high interannual variability in strength, duration, and timing. A second Acidalia and Syrtis cloud abundance amplification in a year may happen; these are weaker than the first event of the year, and we cannot determine any consistent strength, duration, or timing across years. The second Syrtis cloud peak appears to coincide with a Tharsis cloud recovery.

A dynamic, predictive characterization of the ACB state at any time should therefore capture cloud cover over Tharsis, Acidalia, and Syrtis Major. However, clouds over Tharsis show no substantial interannual variability and follow a consistent seasonal evolution. Clouds over Acidalia are almost exclusively captured by EOF2, and Syrtis Major cloud events project on EOF3, 4, and 6, with EOF3 being dominant and explaining the primary Syrtis cloud intensification. Therefore, to track and characterize ACB in-

traseasonal and interannual variability, we propose an operational Aphelion Cloud Belt index (ACB-index, hereafter) based on PC2 and PC3, detailed below.

3.2 ACB-index

While the individual PCs allow us to examine Acidalia and Syrtis Major cloud variability separately, a combined index provides a more convenient way to characterize the evolution of the cloud belt as a whole. In particular, the ACB-index describes both the strength of the combined cloud anomaly and the relative contributions of the two regions through its amplitude and phase, respectively. This allows us to define and compare cloud events consistently in terms of their amplitude, timing, duration, and evolution across Mars Years. We calculate the ACB-index from the 5-sol causal mean non-normalized PC2 and PC3 amplitudes. Instead of normalizing PC2 and PC3 based on their individual mean and standard deviation, we normalize by the mean and standard deviation of the length of the (PC2, PC3) vector (across the historic record of MDGMs). We propose an operational ACB-index to be expressed as the normalized α =(PC2*, PC3*) vector. The normalized PC2* and PC3* become the index coordinates, $A = \sqrt{\mathrm{PC2}^{*2} + \mathrm{PC3}^{*2}}$ is the amplitude and $\phi = \tan^{-1}(\mathrm{PC3}^*/\mathrm{PC2}^*)$ is the phase of the ACB-index. In order to identify high-amplitude cloud events over Acidalia and/or Syrtis, we apply a 1 std radius mask on the phase-amplitude evolution; high-amplitude events are insensitive to this mask. Our underlying assumption behind this mask is that high-intensity cloud cover will always result in an index outside this circle, and that phase is only meaningful to discuss for such high-amplitude events. The evolution of the ACB-index with the 1 std radius mask is shown in Fig. 4.

Apart from MY 29, each cloud event that reached 1 std amplitude occurred at a phase between $\phi = -45°$ and 110°. The amplification typically passes the 1 std threshold between $L_s = 130 - 135°$, with a positive PC2* dominating a weak and negative PC3*, corresponding to an amplified cloud cover over Acidalia and an absence of clouds over Syrtis. The ACB-index transitions to the first quadrant (i.e., positive PC2*, PC3*) typically between $L_s = 135 - 140°$ and undergoes a clockwise, high-amplitude shift towards a weakened PC2* and a strong PC3* between $L_s = 145 - 150°$. Afterward, the cloud belt anomalies weaken and return to 1 std shortly after $L_s = 150°$.

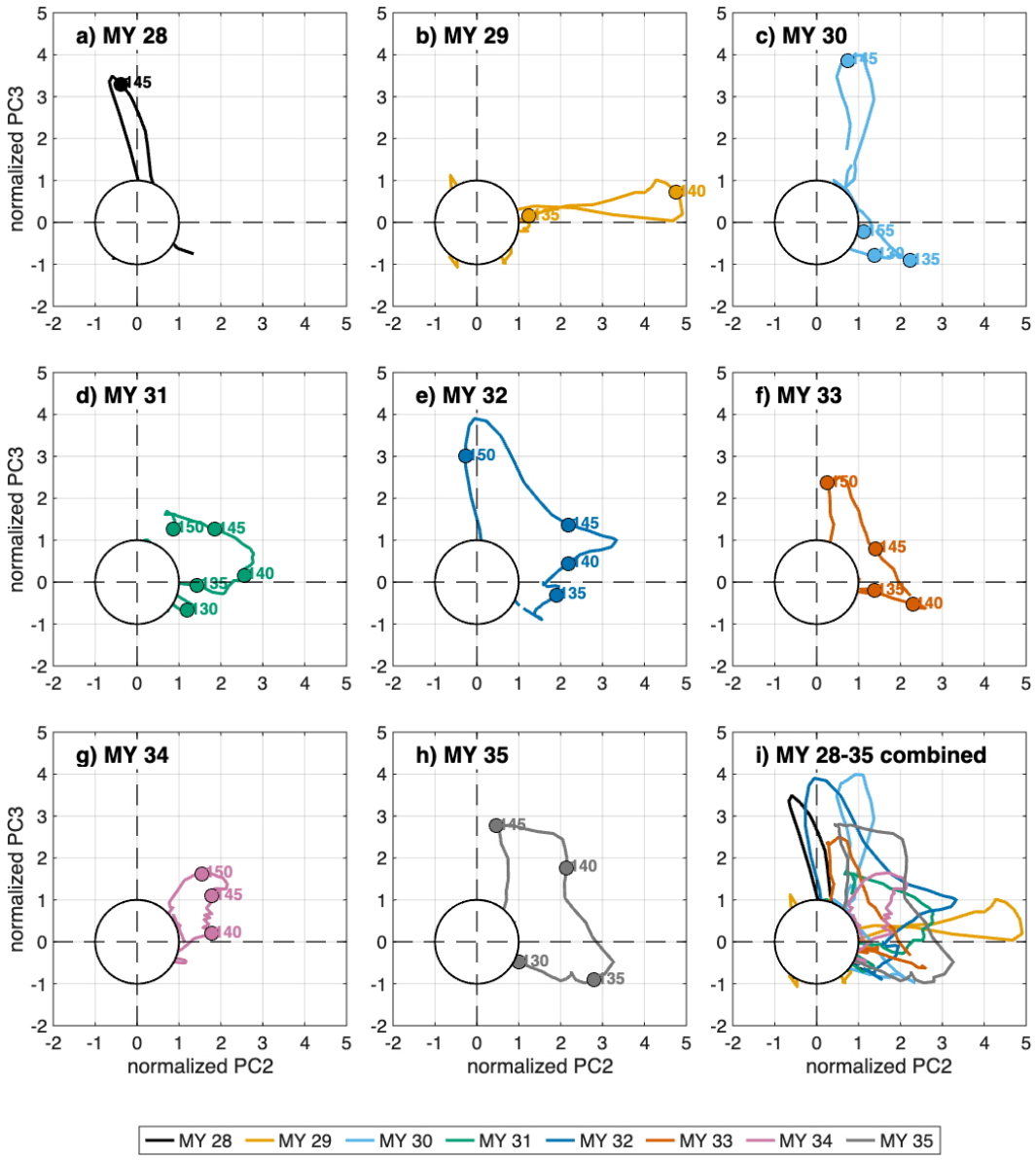


Figure 4: The evolution of the ACB-index over MY 28-35, with a 1 std radius circle mask applied to distinguish high-amplitude cloud events. Panels (a)-(h) show individual years with circle markers at L_s = 135°, 140°, 145°, 150° and 155°. Panel (i) depicts the evolution for all MY 28-35 for direct interannual comparison.

Therefore, the typical lifecycle of high-amplitude cloud anomalies consists of an Acidalia amplification followed by a shared Acidalia/Syrtis cloud event, finally culminating in an intense Syrtis Major but a weakened Acidalia. In the aftermath, cloud anomalies disappear. Two notable exceptions exist in this sequence. First, in MY 28 there was a Syrtis Major amplification, but no Acidalia cloud event preceding it, implying that Syrtis events may not require an Acidalia pre-event. Second, MY 29 included a very strong Acidalia intensification in cloud cover that was not followed by a Syrtis Major cloud strengthening, suggesting that Acidalia events may not imply a forthcoming Syrtis amplification. Overall, MY 28 and 29 show that Acidalia events are neither necessary nor sufficient precursors for Syrtis Major cloud events.

Finally, the secondary cloud events we identified from individual PC evolutions are much weaker in ACB-index amplitude than primary events, and they barely reach the 1-std threshold (which they do, in fact, in e.g. MY 30).

4 Discussion

4.1 Intraseasonal ACB variability is dominated by TCO-like patterns

The EOF analysis shows that the dominant intraseasonal variability of the tropical ACB is organized into a small number of coherent spatial patterns. EOF1 represents the seasonally recurring Tharsis-centered cloud state, EOF2 captures an Acidalia-Arcadia asymmetry, and EOF3 captures a Syrtis Major-Tharsis asymmetry. This structure implies that the visually prominent west-east cloud shifts in the MDGMs are not arbitrary map-to-map variations, but repeated projections onto a low-dimensional set of spatial patterns.

This result supports the interpretation of ACB variability as TCO-dominated, in that the combined evolution of EOFs 1-3 manifests as a tropical cloud abundance shift between preferred longitudinal sectors. However, the results also show that the TCO should not be interpreted as a strictly periodic oscillation with a quasi-fixed period or phase speed. The first major shift of each Mars Year is strongly constrained by the seasonal cycle, whereas later shifts are less regular in timing, amplitude, and duration. The ACB therefore contains both a seasonally locked component and a transient intraseasonal component. Therefore, the TCO is perhaps not best interpreted as a long-period oscillation comprising a

few selected wave modes (that the term TCO would indicate), but rather, a combination of

1. a primary, seasonally evolving cloud shift with no interannual variability — the first EOF1-EOF3 transition with an in-between EOF2 cloud event almost every year — resembling a transition between cloud cover equilibria (Mester, Wilson, & Kahre, 2026),
2. and further secondary, annually distinct EOF3-EOF1 transitions that occur on weekly timescales. These secondary transitions may correspond to fundamental equatorial (i.e., Kelvin or Rossby) waves (Wang et al., 2024).

In particular, to further study equatorial wave-like behavior in the tropical clouds, our PC-analysis suggests that the relevant time window to consider for such waves starts around $L_s = 135°$ and transient PC evolution is sustained at least until $L_s = 180°$, even in years when a second Tharsis-Syrtis shift is not apparent.

The seasonally locked component is most clearly expressed in PC1 and in the early evolution of PC2–PC4. Until approximately $L_s = 131°$, the leading PCs show little interannual variability, indicating that the growth of the Tharsis-centered ACB and the initial Acidalia amplification occur in a highly repeatable seasonal background state. After this time, the PCs diverge more substantially from year to year. This divergence is especially clear in PC3, which controls the dominant Syrtis Major component. Thus, the transition from the early ACB state to the Syrtis Major intensification phase is seasonally favored, but the strength and detailed evolution of the Syrtis Major event are not fixed by season alone.

This distinction is important for the physical interpretation of the TCO. A purely seasonal description would miss the large interannual variability in Syrtis Major cloud intensity. Conversely, treating every shift as an independent transient event would miss the strong seasonal organization of the first event in each Mars Year. The ACB-index is useful because it captures both aspects: it preserves the phase information needed to describe the Acidalia-to-Syrtis transition, while its amplitude quantifies each event's strength relative to the multi-year reference behavior.

4.2 Episodic Syrtis Major cloud intensification

The PC evolution and the ACB-index provide a compact description of episodic Syrtis Major cloud intensification. In most Mars Years, the high-amplitude ACB-index trajectory begins with enhanced Acidalia cloud abundance, corresponding to positive PC2* and weak or negative PC3*. The index then moves into the first quadrant, where both Acidalia and Syrtis Major clouds are enhanced, before rotating toward a state dominated by positive PC3*. This final stage corresponds to the main Syrtis Major cloud intensification.

The primary Syrtis Major events typically peak near $L_s = 143$-$150°$, but their amplitude and duration vary strongly among Mars Years. This behavior suggests that Syrtis Major intensification is a separate stage of the ACB evolution rather than a simple passive consequence of the seasonal decline of Tharsis clouds. The seasonal weakening of Tharsis may provide a favorable background for eastward cloud redistribution or, alternatively, may result from a longitudinal shift in north-south water vapor transport that no longer favors Tharsis. Either case, it does not determine the amplitude and timing of the Syrtis Major event.

The exceptions are particularly informative. MY 28 exhibits Syrtis Major amplification without a clearly resolved preceding Acidalia event. In contrast, MY 29 contains a strong Acidalia event that is not followed by a strong Syrtis Major intensification. These two cases show that Acidalia cloud amplification is neither a necessary nor a sufficient precursor for Syrtis Major cloud intensification. The typical Acidalia-to-Syrtis sequence is therefore a common pathway, but not a deterministic rule.

Secondary Syrtis Major events are weaker and less repeatable than the primary events. Clear secondary peaks appear only in some years, and the separation between primary and secondary events is inconsistent. The projection of Syrtis Major events onto EOF4 also suggests that later events may differ structurally from the first event. The primary Syrtis Major intensification occurs while Tharsis clouds are weakening, whereas later Syrtis Major amplification can be accompanied by a partial recovery of Tharsis cloud abundance. This distinction indicates that the first and later Syrtis Major events may occur under different background circulation states.

4.3 Ghost signal removal

Ghost signal removal is necessary because the raw MDGM record contains strong spectral artifacts near zonal wavenumbers 11-13. These artifacts contaminate the EOF basis, especially the higher EOFs, and can produce spatial patterns that are not physically interpretable as ACB variability. The sequential removal procedure substantially reduces the localized ghost peaks in wavenumber–frequency space and removes the visually obvious wavenumber 11-13 structure from EOFs 4-6.

The removal procedure successfully constructs the ACB-index. The leading EOFs retain their physical interpretation after cleaning: EOF1 remains the Tharsis-centered ACB mode, EOF2 remains the Acidalia mode, and EOF3 remains the dominant Syrtis Major mode. At the same time, the higher modes become more interpretable after removing the ghost pattern. This matters because the ACB-index is based on PC2 and PC3, but interpreting secondary Syrtis Major events also benefits from cleaned higher EOFs.

The procedure is conservative because it targets only the localized spectral neighborhoods associated with the strongest ghost peaks and their conjugates. It should therefore be viewed as an artifact-suppression method rather than a broad spectral filtering of the cloud field. Some sampling-related power may remain outside the targeted regions, and the cleaned MDGM record should not be interpreted as completely free of all observational artifacts. Nevertheless, the disappearance of the dominant wavenumber 11-13 contamination from the EOF patterns demonstrates that the main artifact affecting EOF interpretation has been successfully reduced.

4.4 Usefulness and online calculation of the ACB-index

The rigorous calculation of EOFs, PCs, and the ACB-indices requires the entire historical record of MDGMs and, by construction, need recalculation if the MDGM database is extended. Furthermore, if a new, single (or a handful of) MDGM(s) were to be analyzed, the seasonal mean and hence the respective anomalies (that are projected to the EOF maps) of the cloud field would not be available at hand; hence the construction of PCs and normalized indices would not be possible. For these limitations, we have referred to these versions of PCs and ACB-indices as *offline* versions. To make *online* calculations possible, an accurate approximation of these quantities can be performed as fol-

lows. A major advantage of the *online* ACB-index and EOFs/PCs, described below, is that they can be calculated for newly available MDGMs without recomputing the EOF basis and the ghost signal, and that they do not require information on the seasonal mean, which would disallow online calculations. For the reader's convenience, we provide in the Open Research Section easy-to-use scripts that calculate the PCs and ACB-index from an input RGB-triplet (longitude-latitude) map and its corresponding longitude-latitude grid.

4.4.1 Online calculation of PCs and the ACB-index

The online construction requires calculating several climatological quantities once and storing them beforehand. The climatological quantities are calculated from the current record of MDGMs (MY28-35), including the climatological mean $B_{\rm clim}(\lambda,\theta,t)$ at any longitude-latitude grid point and sol, the ghost EOFs $G_a^{(i)} := \mathrm{EOF}m_{G_a}(\lambda,\theta)$ for $i=1,2$, $a=11,13$, the ghost-removed EOFm and the historical mean μ_m and standard deviation σ_m of the corresponding m-th principal component, $m=1,2,....$ Similarly, the historical mean $\overline{R}$ and standard deviation σ_R of the amplitude of the ACB-index need to be calculated.

For a new MDGM, we first bin the blue-channel field to the same longitude-latitude grid and restrict it to the same tropical domain. To allow *online* calculation of PCs and the ACB-index, anomalies are constructed by removing the corresponding seasonal climatological mean:

$$B'(\lambda,\theta,t) = B(\lambda,\theta,t) - < B_{\rm clim}(\lambda,\theta,t) >, \tag{7}$$

where B is the blue-channel brightness, $B_{\rm clim}$ is an archived climatological mean, $<\cdot>$ denotes seasonal mean, λ is longitude, θ is latitude and t is the sol of observation. This definition of blue-channel anomaly differs crucially from *offline* calculations, where the anomaly was defined as deviations from the seasonal mean in each year (not determinable online), rather than deviations from the multi-year average of the seasonal mean.

We then remove the ghost contribution sequentially using the archived ghost EOFs. First, the anomaly is projected onto the $k=13$ ghost EOFs $G_{13}^{(i)}$, $i=1,2$;

$$c_{13}^{(i)}(t) = \sum_{\lambda,\theta} B'(\lambda,\theta,t) G_{13}^{(i)}(\lambda,\theta) W(\theta), \tag{8}$$

and the projected ghost component is subtracted:

$$B'_{13}(\lambda,\theta,t) = B'(\lambda,\theta,t) - c_{13}^{(1)}(t)G_{13}^{(1)}(\lambda,\theta) - c_{13}^{(2)}(t)G_{13}^{(2)}(\lambda,\theta). \tag{9}$$

The same procedure is then applied to the $k = 11$ ghost EOFs:

$$c_{11}^{(i)}(t) = \sum_{\lambda,\theta} B'_{13}(\lambda,\theta,t)G_{11}^{(i)}(\lambda,\theta)W(\theta), \tag{10}$$

$$B'_{\text{clean}}(\lambda,\theta,t) = B'_{13}(\lambda,\theta,t) - c_{11}^{(1)}(t)G_{11}^{(1)}(\lambda,\theta) - c_{11}^{(2)}(t)G_{11}^{(2)}(\lambda,\theta). \tag{11}$$

Here, $G_{13}^{(i)}$ and $G_{11}^{(i)}$ are the archived ghost EOFs, and $W(\theta) = \sqrt{\cos\theta}$ denotes the spatial weighting used in the EOF construction.

The cleaned anomaly is then projected onto the archived physical EOFs:

$$\text{PC}m(t) = \sum_{\lambda,\theta} B'_{\text{clean}}(\lambda,\theta,t)\text{EOF}m(\lambda,\theta)W(\theta). \tag{12}$$

Subsequently, PCm should be normalized by the mean μ_m and standard deviation σ_m obtained from the historical record, to obtain PCm'. For the ACB-index, the relevant coordinates are PC2 and PC3. We then smooth these PCs using a 5-sol causal mean filter, as done earlier in this study. We denote the smoothed values by $\text{PC2}_5(t)$ and $\text{PC3}_5(t)$. The (PC2_5,PC3_5) vector length is

$$R(t) = \left[\text{PC2}_5(t)^2 + \text{PC3}_5(t)^2\right]^{1/2}. \tag{13}$$

The amplitude is normalized using the archived mean $\overline{R}$ and standard deviation σ_R of R from the reference period:

$$A(t) = \frac{R(t) - \overline{R}}{\sigma_R}. \tag{14}$$

The normalized ACB-index coordinates are then calculated by preserving the direction of the PC2-PC3 vector:

$$\text{PC2}^*(t) = A(t)\frac{\text{PC2}_5(t)}{R(t)}, \tag{15}$$

$$\text{PC3}^*(t) = A(t)\frac{\text{PC3}_5(t)}{R(t)}. \tag{16}$$

The ACB-index amplitude then satisfies

$$A(t) = \left[\text{PC2}^*(t)^2 + \text{PC3}^*(t)^2\right]^{1/2}, \tag{17}$$

and the phase is

$$\phi(t) = \tan^{-1}\left(\frac{\text{PC3}^*(t)}{\text{PC2}^*(t)}\right) \tag{18}$$

In this phase space, positive PC2* indicates an Acidalia-dominated anomaly, while positive PC3* indicates a Syrtis Major-dominated anomaly. The 1 standard deviation circle provides a practical threshold for separating weak background variability from high-amplitude ACB events.

The online version of principal components, and consequently of the ACB-index, is an excellent approximation (see Fig. S1), although is not a perfect fit. The online version assumes that the spatial patterns corresponding to EOFs and ghosts are constant in time; in reality, they are time-dependent. We test the stability of the EOF patterns by recalculating the EOFs after leaving out a Mars Year (cf. (North et al., 1982)). The test concludes more than 95% spatial correlation for each of EOFs 1-4 for any MY left out. This consistency in the patterns further supports the feasibility of online ACB-index calculation. The reader should also note that the online version normalizes the PCs and the ACB-index using specified climatological statistics rather than statistics from the current MY.

This ACB-index and its online formulation are useful for several applications. First, it provides an objective definition of Acidalia and Syrtis Major cloud events based on the index's phase and amplitude. Second, it allows comparison of Mars Years in terms of event timing, amplitude, duration, and recurrence. Third, it provides an observational benchmark for Mars global climate models and reanalyses. A model does not need to reproduce every pixel-scale feature of the MDGMs to be evaluated against observations; it can instead be tested on whether it reproduces the observed ACB-index trajectory. Finally, because the index is causal and can be updated as new MDGMs become available, it provides a practical diagnostic for future Mars weather monitoring and forecast evaluation. However, in order to truly have an online index for tracking the evolution of the ACB, MDGMs would need to be a prepared product each sol. This would require either a fully automated workflow or fixed personnel. Nonetheless, our ACB-index is a starting point for an operational metric to use in Martian weather forecasts.

4.5 Physical implications and limitations

The present analysis does not identify the dynamical mechanism responsible for Syrtis Major cloud intensification, but it constrains any proposed mechanism. First, the mechanism must operate within a strongly seasonally organized background state, be-

cause the first major ACB shift occurs within a narrow seasonal window. Second, it must allow substantial interannual variability, because the amplitude and duration of Syrtis Major events differ strongly across Mars Years. Third, it must explain why strong Acidalia events do not always lead to strong Syrtis Major events and why not all strong Syrtis Major events are preceded by Acidalia events. We note that in MY 29, with no Syrtis Major cloud event, strong dust storm activity occurred (M. Battalio & Wang, 2019) shortly after PC2 amplification, suggesting that dust activity may explain the lack of water-ice cloud intensification over Syrtis.

These constraints argue against interpreting the TCO as a single strictly periodic oscillation. Instead, the observed behavior is more consistent with a seasonally favored transition whose amplitude and recurrence are modulated by transient dynamical, radiative, or microphysical processes (Navarro et al., 2014). The ACB-index provides a way to test these possibilities in future work. For example, temperature, wind, water vapor, dust, tide, or wave diagnostics can be composited by ACB-index phase rather than by L_s alone. This would help separate the seasonal cycle from the cloud-shift state itself.

Several limitations should also be kept in mind. The MDGMs sample the cloud field at approximately 3 pm local time, so the index describes the afternoon ACB state rather than the full diurnal evolution (Wolff et al., 2022; Atwood et al., 2025) of the cloud field. The blue-channel brightness proxies water-ice cloud abundance rather than directly retrieving water-ice optical depth. Missing MDGMs also limit the interpretation of some years, especially when gaps occur near possible secondary events. Finally, because the EOF basis is empirical, the ACB-index should be revalidated if substantially longer MDGM records or new mapping products become available. These limitations do not undermine the usefulness of the ACB-index, but they define the observational framework within which we should interpret its phase and amplitude.

5 Conclusion

We developed a quantitative framework, for diagnosing intraseasonal variability in Mars' Aphelion Cloud Belt using blue-filtered Mars Daily Global Maps from MY 28–35 during Ls = 0–180°. The main conclusions are as follows.

1. The leading EOFs of the tropical blue-channel field capture the dominant spatial structures of the ACB, including the Tharsis-centered cloud state and episodic redistribution of cloud abundance toward Acidalia and Syrtis Major.
2. Ghost peaks (due to spacecraft observation patterns) contaminate the raw EOF basis in wavenumber-frequency space. A conservative sequential spectral-removal procedure reduces these artifacts while preserving the large-scale ACB variability.
3. A phase-amplitude ACB-index constructed from normalized PC anomalies provides a compact quantitative descriptor of the TCO-like cloud evolution.
4. The first major west-east cloud shift of each Mars Year occurs within a narrow seasonal window, suggesting control by the seasonally evolving quasi-stationary circulation.
5. Later shifts are more irregular in timing, amplitude, and duration, indicating a transient intraseasonal component that is not strictly locked to the seasonal cycle.
6. The ACB-index provides an observational benchmark for future studies of Mars water-ice clouds, thermal tides, stationary waves, transient waves, and model simulations of the tropical water cycle.
7. In particular, a future applicability of the PC evolutions and the ACB-index is assessing how well Mars Global Climate Models (MGCMs) and deep learning foundation models (FMs) reproduce the Aphelion Cloud Belt, a critical element of Mars' water cycle.
8. The online formulation of the ACB-index provides a practical metric for future Mars weather prediction, enabling forecasts to be evaluated against the observed phase and amplitude of tropical cloud belt variability.

Open Research Section

The Mars Daily Global Maps used for this study are publicly available at Wang et al. (2020). We provide a NetCDF file together with easy-to-use MATLAB and Python scripts through Zenodo (Mester, Battalio, et al., 2026) that calculate the online ACB-index and PCs for any MDGM image.

Conflict of Interest disclosure

The authors declare there are no conflicts of interest for this manuscript.

Acknowledgments

JMB acknowledges support from Mars Data Analysis Program Grant #80NSSC22K1077. The authors thank two anonymous reviewers for their feedback that helped improve the paper.

References

Atwood, S. A., Smith, M. D., Wolff, M. J., & Edwards, C. S. (2025). The full diurnal cycle of mars water-ice cloud optical depth in emirs observations. *Journal of Geophysical Research: Planets*, *130*(8), e2025JE008961. doi: https://doi.org/10.1029/2025JE008961

Battalio, J. M., Lora, J. M., Lubis, S. W., & Hassanzadeh, P. (2025). Propagation and periodicity of mars's northern annular mode modulates the dust cycle. *Geophysical Research Letters*, *52*(6), e2024GL112814. doi: https://doi.org/10.1029/2024GL112814

Battalio, M., & Wang, H. (2019). The aonia-solis-valles dust storm track in the southern hemisphere of mars. *Icarus*, *321*, 367-378. Retrieved from `https://www.sciencedirect.com/science/article/pii/S0019103518305402` doi: https://doi.org/10.1016/j.icarus.2018.10.026

Battalio, M. J., & Lora, J. M. (2021). Annular modes of variability in the atmospheres of mars and titan. *Nature Astronomy*, *5*, 1139-1147. doi: https://doi.org/10.1038/s41550-021-01447-4

Clancy, R., Grossman, A., Wolff, M., James, P., Rudy, D., Billawala, Y., ... Muhleman, D. (1996). Water vapor saturation at low altitudes around mars aphelion: A key to mars climate? *Icarus*, *122*(1), 36-62. doi: https://doi.org/10.1006/icar.1996.0108

Giuranna, M., Wolkenberg, P., Grassi, D., Aronica, A., Aoki, S., Scaccabarozzi, D., ... Formisano, V. (2021). The current weather and climate of mars: 12 years of atmospheric monitoring by the planetary fourier spectrometer on mars express. *Icarus*, *353*, 113406. (From Mars Express to Exomars) doi: https://doi.org/10.1016/j.icarus.2019.113406

Guha, B. K., Panda, J., & Wu, Z. (2021). Observation of aphelion cloud belt over martian tropics, its evolution, and associated dust distribution from mcs data. *Advances in Space Research*, *67*(4), 1392-1411. doi: https://doi.org/10.1016/j.asr.2020.11.010

Hannachi, A., Jolliffe, I. T., & Stephenson, D. B. (2007). Empirical orthogonal functions and related techniques in atmospheric science: A review. *International Journal of Climatology*, *27*(9), 1119-1152. doi: https://doi.org/10.1002/joc.1499

Hinson, D. P., & Wilson, R. J. (2004). Temperature inversions, thermal tides, and water ice clouds in the martian tropics. *Journal of Geophysical Research: Planets*, *109*(E1). doi: https://doi.org/10.1029/2003JE002129

Hinson, D. P., & Wilson, R. J. (2021). Baroclinic waves in the northern hemisphere of mars as observed by the mro mars climate sounder and the mgs thermal emission spectrometer. *Icarus*, *357*, 114152. doi: https://doi.org/10.1016/j.icarus.2020.114152

Kahre, M., Hollingsworth, J., Haberle, R., & Wilson, R. (2015). Coupling the mars dust and water cycles: The importance of radiative-dynamic feedbacks during northern hemisphere summer. *Icarus*, *260*, 477-480. Retrieved from `https://www.sciencedirect.com/science/article/pii/S0019103514003832` doi: https://doi.org/10.1016/j.icarus.2014.07.017

Khayat, A. S. J., Smith, M. D., Wolff, M. J., Guzewich, S. D., Mason, E. L., & Atwood, S. (2023). The mars atmosphere water ice aerosol climatology by mro/crism: 5 mars years of observations. *Journal of Geophysical Research: Planets*, *128*(7), e2023JE007761. doi: https://doi.org/10.1029/2023JE007761

Lemmon, M. T., Wolff, M. J., Bell, J. F., Hayes, A., & Maki, J. (2025). The perseverance rover's mastcam-z visible aerosol optical depth recor. *AGU25*. Retrieved from `https://agu.confex.com/agu/agu25/meetingapp.cgi/Paper/1911427`

Leroy, S. S., Yung, Y. L., Richardson, M. I., & Wilson, R. J. (2003). Principal modes of variability of martian atmospheric surface pressure. *Geophysical Research Letters*, *30*(13). doi: https://doi.org/10.1029/2002GL015909

Madeleine, J.-B., Forget, F., Millour, E., Navarro, T., & Spiga, A. (2012). The influence of radiatively active water ice clouds on the martian climate. *Geophysical*

Research Letters, *39*(23). doi: https://doi.org/10.1029/2012GL053564

Matthews, A. J. (2000). Propagation mechanisms for the madden-julian oscillation. *Quarterly Journal of the Royal Meteorological Society*, *126*(569), 2637-2651. doi: https://doi.org/10.1002/qj.49712656902

Mester, M., Battalio, J., Kahre, M., & Wilson, R. J. (2026, September). *An online acb-index: Quantifying intraseasonal and interannual variability in mars' aphelion cloud belt. [Dataset]* Zenodo. Retrieved from `https://doi.org/10.5281/zenodo.22249424` doi: 10.5281/zenodo.22249424

Mester, M., Wilson, R. J., & Kahre, M. A. (2026). Radiatively coupled equatorial waves in mars' aphelion cloud belt: Wavenumber–frequency analysis in mars gcm simulations. *Icarus*, *449*, 116967. doi: https://doi.org/10.1016/j.icarus.2026.116967

Montmessin, F., Forget, F., Rannou, P., Cabane, M., & Haberle, R. M. (2004). Origin and role of water ice clouds in the martian water cycle as inferred from a general circulation model. *Journal of Geophysical Research: Planets*, *109*(E10). doi: https://doi.org/10.1029/2004JE002284

Navarro, T., Madeleine, J.-B., Forget, F., Spiga, A., Millour, E., Montmessin, F., & Määttänen, A. (2014). Global climate modeling of the martian water cycle with improved microphysics and radiatively active water ice clouds. *Journal of Geophysical Research: Planets*, *119*(7), 1479-1495. doi: https://doi.org/10.1002/2013JE004550

North, G. R., Bell, T. L., Cahalan, R. F., & Moeng, F. J. (1982). Sampling errors in the estimation of empirical orthogonal functions. *Monthly Weather Review*, *110*(7), 699 - 706. doi: 10.1175/1520-0493(1982)110⟨0699:SEITEO⟩2.0.CO;2

Richardson, M. I., Wilson, R. J., & Rodin, A. V. (2002). Water ice clouds in the martian atmosphere: General circulation model experiments with a simple cloud scheme. *Journal of Geophysical Research: Planets*, *107*(E9), 2-1-2-29. doi: https://doi.org/10.1029/2001JE001804

Smith, M. D. (2004). Interannual variability in tes atmospheric observations of mars during 1999–2003. *Icarus*, *167*(1), 148-165. (Special Issue on DS1/Comet Borrelly) doi: https://doi.org/10.1016/j.icarus.2003.09.010

Smith, M. D. (2019). Local time variation of water ice clouds on mars as observed by themis. *Icarus*, *333*, 273-282. doi: https://doi.org/10.1016/j.icarus.2019.06

.009

Wang, H., Battalio, M., & Huber, Z. (2020). MRO MARCI Mars Daily Global Maps V2.
doi: 10.7910/DVN/U3766S

Wang, H., & González Abad, G. (2021). Cloud masks derived from the mars daily global maps and an application to the tropical cloud belt on mars. *Geosciences*, *11*(8). doi: 10.3390/geosciences11080324

Wang, H., Richardson, M. I., Toigo, A. D., & Newman, C. E. (2024). Large scale oscillations in the martian tropical cloud belt. *Journal of Geophysical Research: Planets*, *129*(10), e2024JE008479. (e2024JE008479 2024JE008479) doi: https://doi.org/10.1029/2024JE008479

Wheeler, M. C., & Hendon, H. H. (2004). An all-season real-time multivariate mjo index: Development of an index for monitoring and prediction. *Monthly Weather Review*, *132*(8), 1917 - 1932. doi: 10.1175/1520-0493(2004)132⟨1917:AARMMI⟩2.0.CO;2

Willame, Y., Neary, L., Daerden, F., Wolff, M. J., Erwin, J. T., Thomas, I. R., ... López-Valverde, M. A. (2026). Ice cloud and dust climatologies over 4 martian years from tgo/nomad-uvis nadir retrieval. *Journal of Geophysical Research: Planets*, *131*(6), e2025JE009633. Retrieved from `https://agupubs.onlinelibrary.wiley.com/doi/abs/10.1029/2025JE009633`

Wilson, R. J., & Guzewich, S. D. (2014). Influence of water ice clouds on nighttime tropical temperature structure as seen by the mars climate sounder. *Geophysical Research Letters*, *41*(10), 3375-3381. doi: https://doi.org/10.1002/2014GL060086

Wilson, R. J., Lewis, S. R., Montabone, L., & Smith, M. D. (2008). Influence of water ice clouds on martian tropical atmospheric temperatures. *Geophysical Research Letters*, *35*(7). doi: https://doi.org/10.1029/2007GL032405

Wilson, R. J., Millour, E., Navarro, T., Forget, F., & Kahre, M. A. (2014). Gcm simulations of aphelion season tropical cloud and temperature structure. *Mars Atmosphere: Modeling and Observations, 5th International Workshop, Oxford, UK.*. Retrieved from `https://www-mars.lmd.jussieu.fr/oxford2014/abstracts/wilson_clouds_oxford2014.pdf`

Wolff, M. J., Clancy, R. T., Kahre, M. A., Haberle, R. M., Forget, F., Cantor, B. A., & Malin, M. C. (2019). Mapping water ice clouds on mars with mro/marci. *Icarus*, *332*, 24-49. doi: https://doi.org/10.1016/j.icarus.2019.05.041

Wolff, M. J., Fernando, A., Smith, M. D., Forget, F., Millour, E., Atwood, S. A., ... Fisher, C. (2022). Diurnal variations in the aphelion cloud belt as observed by the emirates exploration imager (exi). *Geophysical Research Letters*, *49*(18), e2022GL100477. doi: https://doi.org/10.1029/2022GL100477

Yamashita, Y., Kuroda, T., & Takahashi, M. (2007). Maintenance of zonal wind variability associated with the annular mode on mars. *Geophysical Research Letters*, *34*(16). doi: https://doi.org/10.1029/2007GL030069